

# Improved Analytical Model of an Outer Rotor Surface Permanent Magnet Machine for Efficiency Calculation with Thermal Effect

**Author, co-author (Do NOT enter this information. It will be pulled from participant tab in MyTechZone)**

**Affiliation (Do NOT enter this information. It will be pulled from participant tab in MyTechZone)**

## Abstract

In this paper, an improved analytical model accounting for thermal effects in the electromagnetic field solution as well as efficiency map calculation of an outer rotor surface permanent magnet (SPM) machine is described. The study refers in particular to an in-wheel motor designed for automotive electric powertrain. This high torque and low speed application pushes the electric machine close to its thermal boundary, which necessitates estimates of winding and magnet temperatures to update the winding resistance and magnet remanence in the efficiency calculation. An electromagnetic model based on conformal mapping is used to compute the field solution in the air gap. The slotted air-gap geometry is mapped to a simpler slotless shape, where the field solution can be obtained by solving Laplace's equation for scalar potential. The canonical slotless domain solution is mapped back to the original domain and verified with finite element model (FEM) results. Closed form solutions of core loss and magnet loss are derived from the air-gap field solution. The copper loss is calculated by considering the proximity loss and skin effects. In order to estimate the winding and magnet temperatures, a thermal model is built using a lumped parameter thermal network with an improved discretization approach. The model has been validated experimentally using the end-winding and coolant temperatures. The energy consumption calculation with the New European Driving Cycle (NEDC) is performed and the benefit of having the thermal model is quantified in terms of percentage difference in the calculated energy consumptions.

## Introduction

Electric vehicle powertrain components are optimized with a focus on minimizing the energy consumption in a driving cycle, which represents the real world vehicle operation. Analytical models, which are simple and accurate in estimating the powertrain efficiency, can reduce the computational time of the early stage design optimization process. In this paper, an analytical modelling approach for an outer rotor surface mounted permanent magnet (SPM) machine designed for an in-wheel motor electric powertrain is explained in detail.

In literature, the approaches for computing the airgap field solution of the SPM machine, which can be the basis for calculating the efficiency, are given as follows. Carter introduced the use of an equivalent air-gap that is greater than the physical air-gap to model the slotting effect [1,2] in the field solution. This method captures the overall reduction in air-gap flux density, but the local distortion of the flux density which produces cogging torque is not modelled. Zhu et al.[3] proposed a relative permeance based method to model the local radial field distortion. As this method does not include the influence of slotting in the tangential field component, Zarko et al.[4] suggested a complex relative permeance method. The radial and tangential components of the field solution and the permeance function are represented as real and imaginary parts of a complex number, which enabled the derivation of closed form solutions for the global parameters. The harmonic model [5] and mode matching technique [6] give good accuracy with reasonable computation time. The comparison study performed in [7] indicates that the complex permeance and the mode matching techniques provide good compromise between accuracy and computational time. The main

missing topic to be addressed is the study of temperature influence in the efficiency map calculation.

In order to resolve the above mentioned problem, a thermal model based on lumped parameter thermal networks is built using the Distributed Loss & Capacitance (DLC) element as proposed in [8]. The network is solved by introducing the losses obtained from the electromagnetic model and considering the effect of rotational speed on some of the boundary conditions. The temperature affects the properties of magnet and winding in the machine. Radially magnetized neodymium magnet is used in the SPM machine and its remanence reduces with increasing temperature until a maximum allowable point, above which demagnetization of the magnet occurs. On the other hand, the temperature rise increases the DC loss contribution in the total winding loss but reduces the AC loss [9]. The coupled electromagnetic-thermal model discussed in this paper accounts for these effects allowing efficient, due to the reduced computational effort, and improved estimation of the machine losses and performance.

## 1. Mathematical Modelling of Electric Machine

The air gap field solution of the machine, which is the basis for calculating the global parameters such as torque, losses, and efficiency, is obtained through a conformal mapping procedure. The saturation effect is not included in the calculation based on the assumption that the iron is infinitely permeable. The outer rotor surface permanent magnet machine with radial magnetization developed for automotive application is shown in Figure 1 and its cross-sectional view is given in Figure 2.



Figure 1. In-wheel motor assembled in the vehicle.

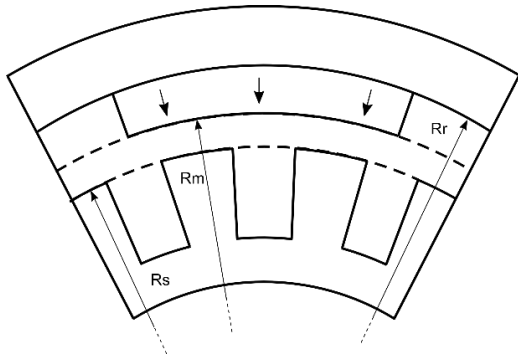


Figure 2. Single pole pitch cross section of outer rotor SPM motor.

The motor parameters are given in Table 1. However, due to confidentiality reasons, the dimensions of the motor are not given in the paper

Table 1. Parameters of external rotor surface PM motor

Continuous maximum power	52 kW
Continuous maximum torque	500 Nm
Rated voltage	320 V
Rated current	150 A
Number of poles	40
Number of slot	120
Number of conductor	8

### 1.1. Electromagnetic Torque calculation

The field produced by the permanent magnets in the slotted air gap ( $B_s$ ) is computed from the slotless air-gap field solution ( $B_k$ ) and complex relative air-gap permeance ( $\lambda$ ) as in (1). The term  $\lambda$  accounts for slotting effect in the field solution [10, 11].

$$B_s = B_k \lambda^* \quad (1)$$

$$B_{sr} + jB_{s\theta} = (B_{kr}\lambda_a + B_{k\theta}\lambda_b) + j(B_{k\theta}\lambda_a - B_{kr}\lambda_b) \quad (2)$$

where  $r$  and  $\theta$  denotes the radial and tangential components of the field solutions. Similarly,  $\lambda_a$  and  $\lambda_b$  in (2) capture the slotting effect in the radial and tangential directions.

Conformal transformation, a special kind of complex function that preserves the angle between intersecting curves at all points in the mapped complex variable planes, is employed as the perpendicularity between equipotential lines and flux paths should be preserved for magnetostatic calculations. The slotted air gap shape (S plane) is transformed into a slotless air gap (K plane) using four different conformal mapping functions as shown in Figure 3.

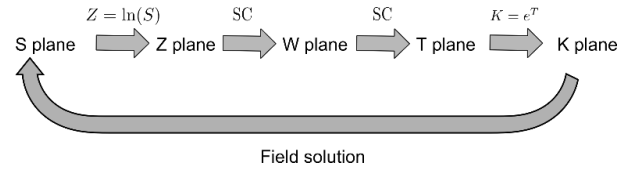


Figure 3. Analytical conformal mapping sequence.

The closed form field solution of slotless air gap field was derived by Zhu et al. in [10].

$$B_{str} = \sum_{n=1,3,\dots}^{\infty} \frac{(-4npB_r \sin \frac{n\pi\alpha_p}{2})}{n\pi\mu_r((np)^2 - 1)} \left[ \left( \frac{r}{R_m} \right)^{np-1} + \left( \frac{R_s}{R_m} \right)^{np-1} \left( \frac{R_s}{r} \right)^{np+1} \right]$$

$$\left\{ \frac{(np-1) \left( \frac{R_m}{R_r} \right)^{2np} + 2 \left( \frac{R_m}{R_r} \right)^{np-1} - (np+1)}{\frac{\mu_r+1}{\mu_r} \left[ 1 - \left( \frac{R_s}{R_r} \right)^{2np} \right] - \frac{\mu_r-1}{\mu_r} \left[ \left( \frac{R_s}{R_m} \right)^{2np} - \left( \frac{R_m}{R_r} \right)^{2np} \right]} \right\} \cos(np\theta)$$

$$B_{st\theta} = \sum_{n=1,3,\dots}^{\infty} \frac{(-4npB_r \sin \frac{n\pi\alpha_p}{2})}{n\pi\mu_r((np)^2 - 1)} \left[ - \left( \frac{r}{R_m} \right)^{np-1} + \left( \frac{R_s}{R_m} \right)^{np-1} \left( \frac{R_s}{r} \right)^{np+1} \right]$$

$$\left\{ \frac{(np-1) \left( \frac{R_m}{R_r} \right)^{2np} + 2 \left( \frac{R_m}{R_r} \right)^{np-1} - (np+1)}{\frac{\mu_r+1}{\mu_r} \left[ 1 - \left( \frac{R_s}{R_r} \right)^{2np} \right] - \frac{\mu_r-1}{\mu_r} \left[ \left( \frac{R_s}{R_m} \right)^{2np} - \left( \frac{R_m}{R_r} \right)^{2np} \right]} \right\} \sin(np\theta) \quad (3)$$

and where  $np=1$ ,

$$B_{str} = \sum_{n=1,3,\dots}^{\infty} \frac{2npB_r \sin \frac{n\pi\alpha_p}{2}}{n\pi\mu_r} \left[ 1 + \left( \frac{R_s}{r} \right)^2 \right] \left\{ \frac{\left( \frac{R_m}{R_s} \right)^2 - \left( \frac{R_r}{R_s} \right)^2 + \left( \frac{R_r}{R_s} \right)^2 \ln \left( \frac{R_m}{R_r} \right)^2}{\left( \frac{\mu_r + 1}{\mu_r} \right) \left[ 1 - \left( \frac{R_r}{R_s} \right)^2 \right] - \frac{\mu_r - 1}{\mu_r} \left[ \left( \frac{R_m}{R_s} \right)^2 - \left( \frac{R_r}{R_m} \right)^2 \right]} \right\} \cos(\theta)$$

$$B_{st\theta} = \sum_{n=1,3,\dots}^{\infty} \frac{2npB_r \sin \frac{n\pi\alpha_p}{2}}{n\pi\mu_r} \left[ -1 + \left( \frac{R_s}{r} \right)^2 \right] \left\{ \frac{\left( \frac{R_m}{R_s} \right)^2 - \left( \frac{R_r}{R_s} \right)^2 + \left( \frac{R_r}{R_s} \right)^2 \ln \left( \frac{R_m}{R_r} \right)^2}{\left( \frac{\mu_r + 1}{\mu_r} \right) \left[ 1 - \left( \frac{R_r}{R_s} \right)^2 \right] - \frac{\mu_r - 1}{\mu_r} \left[ \left( \frac{R_m}{R_s} \right)^2 - \left( \frac{R_r}{R_m} \right)^2 \right]} \right\} \sin(\theta) \quad (4)$$

The magnet temperature affects the remanence ( $B_r$ ) in (3), (4) as well as the resulting field solution. The complex relative air-gap permeance introduced for an inner rotor machine using conformal mapping by Zarko et al in [11] is recalculated for the outer rotor machine and the generic expression is given as,

$$\lambda^* = \left( \frac{\partial k}{\partial s} \right)^* = \left( \frac{\partial k}{\partial t} \frac{\partial t}{\partial w} \frac{\partial w}{\partial z} \frac{\partial z}{\partial s} \right)^* \quad (5)$$

Each partial derivative in (5) is defined by the conformal transformation shown in Figure 3 and the final expression of the complex relative permeance [11] can be written as

$$\lambda = \lambda_a + j\lambda_b = \left( \frac{k}{s} \frac{(w-1)}{(w-a)^{\frac{1}{2}}(w-b)^{\frac{1}{2}}} \right) \quad (6)$$

The assumptions made in this method is that the evaluation points form a circular arc in the canonical domain and the magnets retain their shape. Although these assumptions enable the derivation of the closed form solutions of global parameters, they impair the accuracy of the tangential component of field solution, in Figure 5, and the cogging torque. However, the mean torque value obtained from this method is accurate as the radial component of the field solution confirms the FEM result as shown in Figure 4.

The flux linkage ( $\Psi_{pm-ph}$ ) of the phase winding is obtained by integrating the radial flux density across one coil pitch and multiplying it with the number of coils in series ( $N_s$ ) [4]. The distribution factor and pitch factor of the winding scheme for this particular motor are equal to one.

$$\Psi_{pm-ph} = N_s l_a r \int_{-\frac{\gamma_c}{2}}^{+\frac{\gamma_c}{2}} B_{sr}(r, \theta, t) d\theta \quad (7)$$

The stator flux linkage in the  $d$  axis ( $\Psi_d$ ) is the sum of permanent magnet flux linkage in  $d$  axis ( $\psi_{pm-d}$ ), which is derived from Park transformation of the flux linkages in three phase windings, and the contribution from the  $d$ -axis current.

$$\psi_d = \psi_{pm-d} + L_d I_d \quad (8)$$

In the surface mounted permanent magnet machine, the inductance variation in the  $d$ - $q$  axes is negligible ( $L_d = L_q = L_s$ ), so the electromagnetic torque is computed from the flux linkage in the  $d$  axis ( $\Psi_d$ ) and the stator current in  $q$  axis ( $I_q$ ) [12].

$$T_{em} = \frac{3p}{2} \psi_d I_q \quad (9)$$

For the purpose of efficiency calculation, the  $I_q$  current required to produce the demanded output torque is calculated from (9). In the field weakening region the  $I_d$  current is supplied based on the operating speed of the motor as derived in (10) [12].

$$I_d = \frac{\psi_d^2 + L_s^2 I_{max}^2}{2L_s \psi_d} \left[ \left( \frac{\omega_s^A}{\omega} \right)^2 - 1 \right] \quad (10)$$

where  $L_s$  is the stator inductance and  $I_{max}$  is the maximum stator current. The maximum voltage ( $V_s^{max}$ ) defines the rated speed of the motor  $\omega_s^A$  as shown in Figure 6.

$$\omega_s^A = V_s^{max} / \sqrt{(L_s I_q)^2 + (\psi_{pm} + L_s I_d)^2} \quad (11)$$

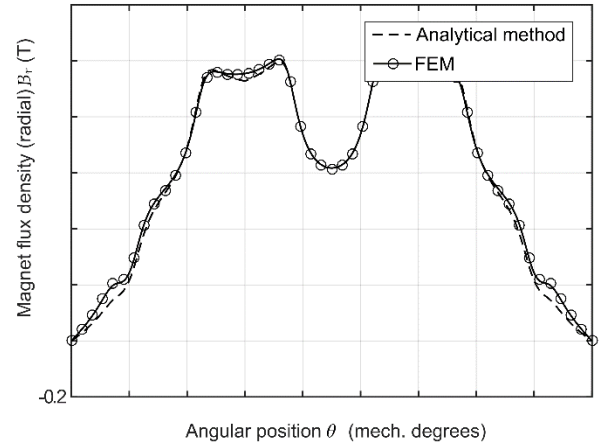


Figure 4. Comparison of radial flux density with FEM result

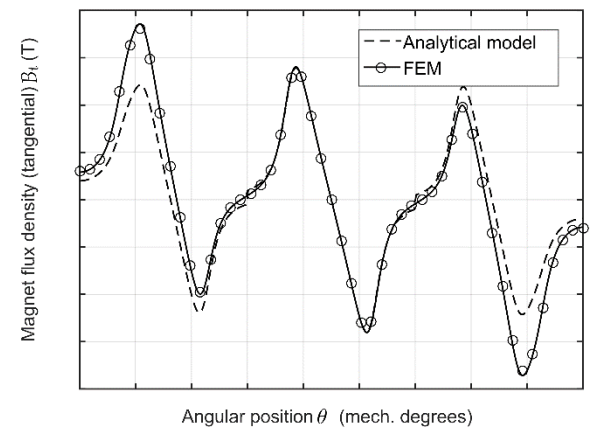


Figure 5. Comparison of tangential flux density with FEM result

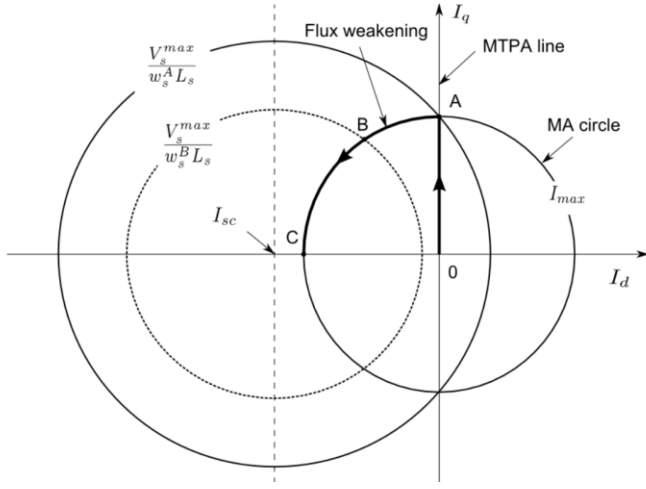


Figure 6. Current locus diagram of outer rotor surface permanent magnet machine with short-circuit current ( $I_{sc}$ ) greater than maximum allowable stator current ( $I_{max}$ )

## 1.2. Efficiency calculation

The efficiency of the motor is defined as the ratio between output power at the shaft ( $P_{out}$ ) and the input electrical power ( $P_{in}$ )

$$\eta = \frac{P_{out}}{P_{in}} \quad (12)$$

The output power is calculated by subtracting the core losses ( $P_c$ ), magnet losses ( $P_{pm}$ ) and mechanical losses ( $P_{ml}$ ) from the electromagnetic power ( $P_{em}$ ).

$$P_{out} = P_{em} - P_c - P_{pm} - P_{ml} \quad (13)$$

The input power ( $P_{in}$ ) is calculated by adding the armature loss ( $P_a$ ) with the electromagnetic power ( $P_{em}$ ).

$$P_{in} = P_{em} + P_a \quad (14)$$

### 1.2.1. Copper losses

The copper loss model includes AC losses due to skin effect inside conductors and additional losses due to proximity effect. It also captures the effect of winding temperature on the losses.

$$P_a = 3 I_s^2 R_{AC} + P_{proximity} \quad (15)$$

The effective resistance ( $R_{AC}$ ) that accounts for the skin effect in the conductor is modelled as a function of conductor dimensions, operating frequency and winding temperature. The conductors are layered in the slot as shown in Figure 7. The detailed explanation of the model can be found in [13].

$$R_{AC} = K_{AC} N_s \frac{1}{\sigma_0} \frac{2(l_a + l_{ew})}{A_c} (1 + \beta_t(T - T_0)) \quad (16)$$

The AC loss factor  $K_{AC}$  can be modelled as,

$$K_{AC} = \left( \frac{360 + 3\gamma^4}{360 + \gamma^4} + \left( \frac{\sum_{l=1} N_l}{N_l I_0} \right)^2 \frac{2\gamma^4}{24 + \gamma^4} \right)$$

where  $\sum_{l=1} N_l$  and  $N_l$  are defined according to Figure 7 [13],  $I_0$  is the current in layer  $l$ ,  $N_s$  is the number coils connected in series,  $\sigma_0$  is the conductivity of copper at reference temperature ( $T_0 = 20^\circ C$ ),  $l_a$  is the stack length,  $l_{ew}$  is the end winding length,  $A_c$  is the cross sectional area of the wire, and  $T$  is the winding temperature. The characteristic dimension  $\gamma$  and the AC loss temperature coefficient  $\beta_t$  are defined as

$$\gamma = 0.93 \sqrt{\epsilon_l} \frac{D_c}{\delta} \quad (17)$$

$$\beta_t = \alpha_t - \alpha_t \frac{1}{k_{AC}} \left( \frac{\sum_{l=1} N_l}{N_l I_0} \right)^2 \frac{384\gamma^4}{(24 + \gamma^4)^2} \quad (18)$$

where  $\epsilon_l$  is the slot fill ratio,  $D_c$  is the diameter of the conductor,  $\delta$  is the skin depth,  $\alpha_t$  is the temperature coefficient of the conductor material. The induced conductor proximity loss from the enclosed ampere turns is given by

$$P_{proximity} = \frac{2l_a}{\rho D_c^2} \left( \frac{\sum_{l=1} N_l}{N_l I_0} \right)^2 \frac{2\gamma^4}{24 + \gamma^4} \quad (19)$$

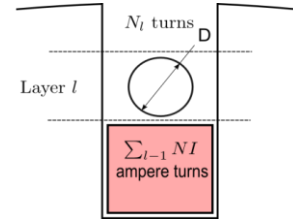


Figure 7. Winding arrangement considered for the copper loss calculation

### 1.2.2. Iron losses

The eddy current and hysteresis losses induced by the permanent magnet flux variation in the stator back-iron are considered in this model and the iron losses in the rotor are neglected. A generic expression for the iron losses considering the effect of harmonics of the flux density can be written in the form [14]

$$P_c = \left[ k_h f B_m^{a_h + b_h B_m} + k_e f^2 \sum_n n^2 B_n^2 \right] \rho_c V_c. \quad (20)$$

where  $k_h$  is the hysteresis loss coefficient,  $k_e$  is the eddy current loss coefficient,  $f$  is the electrical frequency,  $B_m$  is the peak value of flux density waveform and  $B_n$  represents the Fourier coefficients of the flux density waveform. The coefficients  $a_h$  and  $b_h$  are determined by curve fitting the steel lamination data provided by manufacturers.

The harmonic flux components in the stator tooth  $\phi_{tsn}$  are obtained by integrating the harmonic components of radial field solution of the permanent magnet across a slot pitch [14].

$$\phi_{tsn} = l_a R \int_{-\frac{\pi}{Q_s}}^{+\frac{\pi}{Q_s}} B_{srn}(R, \theta, t) d\theta \quad (21)$$

The relationship between the tooth and yoke flux in the frequency domain [14] is given as

$$|\phi_{tsn}| = |\phi_{ysn}| 2 \sin\left(np \frac{\pi}{Q_s}\right). \quad (22)$$

The flux densities in the tooth and yoke regions are then calculated by dividing the corresponding fluxes with their cross sectional areas. A generic form of the flux density calculation is given as

$$B_n = \frac{\phi_n}{A} \quad (23)$$

Form the Fourier coefficients, the time domain waveforms of flux density in the tooth and yoke regions are derived.

$$B = \sum_n B_n \cos(n\omega t) \quad (24)$$

The term  $B_m$  is obtained by taking the maximum value of flux density

$$B_m = \max\left(\sum_n B_n \cos(n\omega t)\right) \quad (25)$$

and the eddy current loss component in (20) is obtained from

$$\left(\frac{dB}{dt}\right)_{rms}^2 = 2\pi^2 f^2 \sum_n n^2 B_n^2 \quad (26)$$

### 1.2.3. Magnet loss

Space harmonics in the armature winding magnetomotive force (MMF) distribution and time harmonics in the current waveform, together with the harmonics in the air gap permeance function due to slotting, create field components which do not rotate in synchronism with the rotor. Consequently, these field harmonics induce eddy currents in the rotor magnets and generate power losses.

Eddy currents induced in the rotor magnet due to  $n^{\text{th}}$  harmonic component of the armature field satisfy the Helmholtz equation which can be written in 2-D polar coordinates in the phasor form

$$\begin{aligned} \frac{\partial^2 \tilde{J}_{zn}}{\partial r^2} + \frac{1}{r} \frac{\partial \tilde{J}_{zn}}{\partial r} + \frac{1}{r^2} \frac{\partial^2 \tilde{J}_{zn}}{\partial \theta'^2} &= k_n^2 \tilde{J}_{zn} \\ k_n^2 &= j\omega_n \mu_{PM} \sigma_{PM} \\ \theta' &= \theta - \omega_{rm} t \end{aligned} \quad (27)$$

where  $\mu_{PM}$  and  $\sigma_{PM}$  are the permeability and electric conductivity of the permanent magnet respectively,  $n$  is the harmonic order of the armature winding field component which induces eddy currents,  $\omega_n$  is the frequency of the  $n^{\text{th}}$  harmonic,  $\theta'$  and  $\theta$  are the angular positions of a point on the magnet surface with respect to the rotor and stator respectively, and  $\omega_{rm}$  is the rotor mechanical speed. The general solution of (27) is given by [7]

$$\begin{aligned} \tilde{J}_{zn}(r, \theta') &= \sum_{m=0}^{\infty} [A_m I_m(k_n r) + B_m K_m(k_n r)] [C_m \cos(m\theta') \\ &\quad + D_m \sin(m\theta')] \end{aligned} \quad (28)$$

where  $I_m$  and  $K_m$  are the modified Bessel functions of the first and second kind of order  $m$  respectively, while  $A_m$ ,  $B_m$ ,  $C_m$  and  $D_m$  are the

constants. Combining (28) with the relationship between radial and tangential components of the magnetic field intensity in the magnet and the induced eddy currents

$$\begin{aligned} \nabla \times \mathbf{J}_n &= \frac{1}{r} \frac{\partial \tilde{J}_{zn}}{\partial \theta'} \mathbf{a}_r - \frac{\partial \tilde{J}_{zn}}{\partial r} \mathbf{a}_{\theta}, \\ &= -\underbrace{j\omega_n \mu_{PM} \sigma_{PM}}_{k_n^2} (\tilde{H}_{rn} \mathbf{a}_r + \tilde{H}_{\theta n} \mathbf{a}_{\theta}), \end{aligned} \quad (29)$$

the following equations are obtained

$$\begin{aligned} \tilde{H}_{rn}(r, \theta') &= -\frac{m}{k_n^2 r} \sum_{m=0}^{\infty} [A_m I_m(k_n r) \\ &\quad + B_m K_m(k_n r)] [-C_m \sin(m\theta') \\ &\quad + D_m \cos(m\theta')] \end{aligned} \quad (30)$$

$$\begin{aligned} \tilde{H}_{\theta n}(r, \theta') &= \frac{1}{k_n} \sum_{m=0}^{\infty} [A_m I'_m(k_n r) + B_m K'_m(k_n r)] [C_m \cos(m\theta') \\ &\quad + D_m \sin(m\theta')] \end{aligned} \quad (31)$$

where  $I'_m$  and  $K'_m$  are the derivatives of Bessel functions. Similar relations can be written for flux density as well since

$$\tilde{B}_n = \mu_{PM} \tilde{H}_n \quad (32)$$

The unknown constants are determined by applying boundary conditions on the rotor and magnet surfaces, i.e.

$$\tilde{H}_{\theta' nII}(R_r, \theta') = 0 \quad (33)$$

$$\tilde{B}_{rnl}(R_m, \theta') = \tilde{B}_{rnlI}(R_m, \theta')$$

where I and II denote the air gap and magnet regions respectively, while  $R_r$  and  $R_m$  are the radii of rotor and magnet respectively. The radial component of flux density on the magnet surface produced by the armature winding currents consists of the direct component ( $\tilde{B}_{rn1}$ ) forming a wave which rotates in the same direction as the rotor and inverse component ( $\tilde{B}_{rn2}$ ) which rotates in the opposite direction of the rotor. The phasors of these two components are defined according to

$$\tilde{B}_{rn1}(r, \theta') = \tilde{C}_{r1n} [\cos(n\theta') - j \sin(n\theta')] \quad (34)$$

$$\begin{aligned} \tilde{C}_{r1n} &= N_c B_{arn}(R_m) \frac{1}{2} I_{\max} \sum_{i=1}^{\frac{Q_s}{3}} \left[ \text{sgn}_{Ai} e^{jn\alpha_{Ai}} \right. \\ &\quad \left. + \text{sgn}_{Bi} e^{j(n\alpha_{Bi} - \frac{2\pi}{3})} \right. \\ &\quad \left. + \text{sgn}_{Ci} e^{j(n\alpha_{Ci} + \frac{2\pi}{3})} \right] \\ \tilde{B}_{rn2}(r, \theta') &= \tilde{C}_{r2n} [\cos(n\theta') + j \sin(n\theta')] \quad (35) \\ \tilde{C}_{r2n} &= N_c B_{arn}(R_m) \frac{1}{2} I_{\max} \sum_{i=1}^{\frac{Q_s}{3}} \left[ \text{sgn}_{Ai} e^{-jn\alpha_{Ai}} \right. \\ &\quad \left. + \text{sgn}_{Bi} e^{j(-n\alpha_{Bi} - \frac{2\pi}{3})} \right. \\ &\quad \left. + \text{sgn}_{Ci} e^{j(-n\alpha_{Ci} + \frac{2\pi}{3})} \right] \end{aligned}$$

where  $B_{arn}$  are the Fourier coefficients of the radial component of flux density on the magnet surface ( $r = R_m$ ) produced by a single coil of the armature winding with one turn ( $N_c=1$ ),  $I_{\max}$  is the peak value of the current waveform (the phase current is assumed to be sinusoidal),

$\text{sgn}A_i, \text{sgn}B_i, \text{sgn}C_i$  are the signs (+ or -) considering the referent orientation of the coil turns in phases A, B and C around the perimeter of the stator,  $\alpha_{Ai}, \alpha_{Bi}, \alpha_{Ci}$  are the phase shifts of the field distributions of individual coils considering their position around the stator perimeter with respect to the referent coil ( $\alpha_{A1}=0$ ). Details about armature winding field solution used in (34) and (35) are provided in [15]. By combining the terms (30), (32), (33), (34) and (35) separately for direct and inverse field components, the unknown constants are obtained.

$$m = n \quad (36)$$

$$C_m = \begin{cases} j & \text{(for direct component)} \\ -j & \text{(for inverse component)} \end{cases} \quad (37)$$

$$D_m = 1 \quad (38)$$

$$A_{nl} = -\frac{\tilde{C}_{rln} \frac{k_{nl}^2 R_m}{n \mu_{PM}} K'_n(k_{nl} R_r)}{K'_n(k_{nl} R_r) I_n(k_{nl} R_m) - K_n(k_{nl} R_m) I'_n(k_{nl} R_r)} \quad (39)$$

$$B_{nl} = \frac{\tilde{C}_{rln} \frac{k_{nl}^2 R_m}{n \mu_{PM}} I'_n(k_{nl} R_r)}{K'_n(k_{nl} R_r) I_n(k_{nl} R_m) - K_n(k_{nl} R_m) I'_n(k_{nl} R_r)} \quad (40)$$

In (39) and (40) the subscript  $l=1$  is used for direct component and  $l=2$  is used for inverse component. The following is also valid

$$k_{n1}^2 = j(\omega - n\omega_{rm}) \mu_{PM} \sigma_{PM} \quad (41)$$

$$k_{n2}^2 = j(\omega + n\omega_{rm}) \mu_{PM} \sigma_{PM} \quad (42)$$

The power dissipated inside the magnet volume is equal to the real part of the integral of average Poynting vector across magnet surface, i.e.

$$P_{PM} = \text{Re} \left\{ \int_S \frac{1}{2} \left( \frac{\tilde{J}}{\sigma_{PM}} \times \tilde{H}^* \right) \cdot \mathbf{n} dS \right\} \\ = 2p \sum_{l=1}^2 \sum_{n=1}^{N_a} \text{Re} \left\{ \int_{-\alpha_p \frac{\pi}{2p}}^{\alpha_p \frac{\pi}{2p}} \frac{1}{2} \frac{\tilde{J}_{znl}}{\sigma_{PM}} \tilde{H}_{\theta ml}^* R_m l_a d\theta' \right\} \quad (43)$$

where  $N_a$  is the maximum order of Fourier coefficients in the armature winding field solution. After substituting (28) and (31) into (43) and performing integration, the final expression for magnet losses is

$$P_{PM} = 2p \sum_{l=1}^2 \sum_{n=1}^{N_a} \text{Re} \left\{ \frac{1}{2\sigma_{PM}} [A_{nl} I_n(k_{nl} R_m) + B_{nl} K_n(k_{nl} R_m)] \cdot \left[ \frac{1}{k_{nl}} (A_{nl} I'_n(k_{nl} R_m) + B_{nl} K'_n(k_{nl} R_m)) \right]^* R_m l_a \alpha_p \frac{\pi}{p} \right\} \quad (44)$$

#### 1.2.4. Mechanical loss

The mechanical losses include frictional losses in the bearings ( $P_{fr}$ ) and windage losses ( $P_{wind}$ ). The frictional losses can be calculated using an empirical formula [16].

$$P_{fr} = k_{fb} m_r n_r 10^{-3} \quad (45)$$

where the empirical constant  $k_{fb}$  varies from 1 to 3,  $m_r$  is the mass of rotor, and  $n_r$  is the speed in rpm. Similarly, the windage losses are defined [16] as

$$P_{win} = 2 D_{ro}^3 l_a n_r^3 10^{-6} \quad (46)$$

where  $D_{ro}$  is the rotor outer diameter and  $l_a$  is the stack length.

### 1.3. Thermal model

Thermal modelling of electrical machine is usually performed by solving the heat equation (47) with desired boundary conditions [17]

$$c \dot{T} = k \nabla^2 T + \dot{q} \quad (47)$$

where  $T$  refers to temperature,  $c$  is the product ( $c = c_p \rho$ ) of specific heat capacity ( $c_p$ ) and mass density ( $\rho$ ),  $k$  is the thermal conductivity, and  $\dot{q}$  is the specific heat generation. In this work, the thermal model is built based on a lumped parameter thermal network (LPTN) in order to have reduced computation effort. The LPTN is created by discretizing each component of the SPM machine into small elements that are further divided into nodes. The nodes are connected to each other through thermal resistors which simulate heat conduction, convection, and radiation as in Figure 8. Hence, the equation (47) can be rewritten (48) as

$$C \dot{T} = \Delta T / R_{cond} + \dot{Q} \quad (48)$$

where  $R_{cond}$  is the conductive thermal resistance [18] and  $\Delta T$  is the temperature gradient between the neighboring nodes. The temperatures of each node is estimated using (48) and the central node, in Figure 8, provides the average temperature of the element when the Biot number (Bi),  $Bi = \frac{l_{ref} h}{k}$  with  $h$  heat transfer coefficient and  $l_{ref}$  element reference length, associated with the element is less than 0.1.

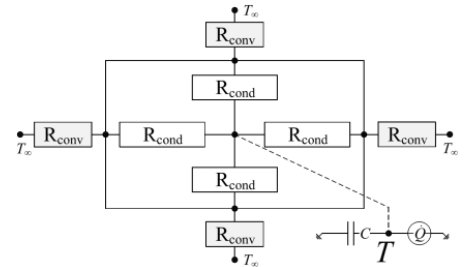


Figure 8. Classic element discretization using a LPTN

Since this condition is not satisfied in all the elements, e.g. end winding where the convective heat transfer changes with the rotor speed, the machine is discretized using the DLC element [8]. As shown in Figure 9, the element is divided into five nodes where the losses and the capacitance are injected according to the ratios given in (49) and (50) respectively.

$$\dot{Q}_c = 0.6 \dot{Q}, \quad \dot{Q}_i = 0.4 \frac{A_i}{A_{ext}} \dot{Q}, \quad (49)$$

$$C_c = 0.6 C, \quad C_i = 0.4 \frac{A_i}{A_{ext}} C, \quad (50)$$

where the subscripts  $c$  and  $i$  represent the central node and  $i^{\text{th}}$  node on an edge of the element respectively, and  $A_i$  is the area exposed to convection that is captured by the  $i^{\text{th}}$  node. As explained in [8], this discretization approach estimates the central element temperature directly and accurately. Moreover, the accuracy of this estimation is good over a large range of Bi, up to  $Bi = 2$  [19].



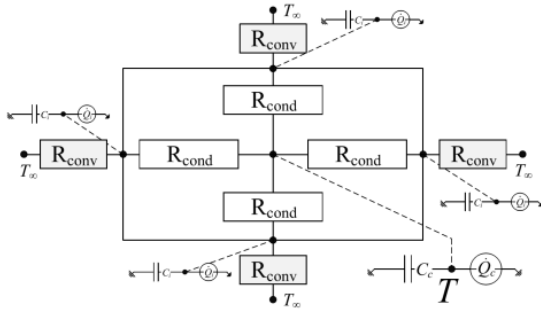


Figure 9. The distributed loss and capacitance (DLC) element

Following this discretization approach, the LPTN of the SPM machine is created as depicted in Figure 10, where a single slot of the machine is shown. The figure indicates how the machine is discretized using rectangular elements in the  $r - \theta$  plane, and axis-symmetric cylindrical elements in the  $r - z$  plane. The machine is cooled with a peripheral water jacket where the water is running tangential to the stator inner surface. The coolant is a 50% water-glycol mixture flowing in four parallel channels of the water jacket. The windings are potted with high thermal conductive epoxy for the improved thermal performance of the machine and they are homogenized following the method presented in [20]. The thermal resistors in the network are calculated from the motor geometry and material properties. Further details regarding the thermal resistors and modelling of conduction and convection heat transfers are provided in [8].

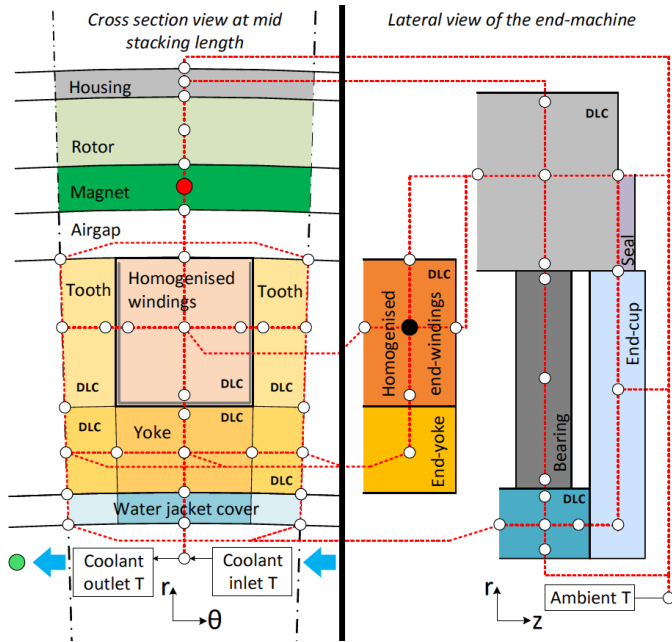


Figure 10. SPM machine nodal discretization using the DLC element

#### 1.4. Solution method

There are various approaches to solve the network presented in the previous section. Object-oriented software such as Matlab Simulink and Modelica [21,22] is normally preferred, since the network can be built using the available elements in their libraries. However, in order to reduce the computation time as much as possible, the linear system of equations can be written directly in Matlab to avoid the pre-

calculations required by the object oriented software. The steady-state temperatures of the machine can be obtained by solving the system in (51), which is derived from (48),

$$[G][T] = -[\dot{Q}] \quad (51)$$

where  $[\dot{Q}]$  is the heat input vector including all the nodal losses and boundary conditions,  $[T]$  is the temperature vector with  $m$  unknowns (number of nodes), and  $[G]$  is the symmetric conductance matrix ( $m \times m$ ) containing the diagonal elements  $G_{i,i} = \sum_j 1/R_{i,j}$  and the remaining elements  $G_{i,j} = -1/R_{i,j}$ . The term  $R_{i,j}$  represents the thermal resistance between the  $i^{\text{th}}$  and  $j^{\text{th}}$  nodes. In order to integrate the system in time, the backward Euler method is implemented to ensure numerical stability. The capacitance matrix  $[C]$  is built with the nodal thermal capacitances along the diagonal; the time integration is performed with a fixed time step  $\delta$  (e.g. 1 sec) as

$$[C] \frac{[T]^\tau - [T]^{\tau-1}}{\delta} = [G][T]^\tau + [\dot{Q}] \quad (52)$$

where  $\tau$  generic time instant. At each time step the vector  $[\dot{Q}]$  is updated depending on the nodal temperatures, e.g., the winding loss that changes conductor resistance. The same effects can be included in (51) with a few iterations of the solution.

#### 1.5. Model validation

The experimental validation is based on DC current excitation of the phases in locked rotor condition. Due to the presence of the water jacket, the heat flow occurs mainly from the windings to the coolant, which also implies that the winding temperature is not significantly influenced by the rotational speed of the motor. The accuracy of the model is confirmed for different coolant flow rates and current values, so the model can be used to estimate the winding temperature in quasi-static analysis of a driving cycle. As an example, the results for the case of 111/min are presented in Figure 11 and Figure 12. In Figure 11, the measured and simulated temperatures of the end-windings are compared. The thermistors (NTC sensors with the accuracy  $0.1^\circ\text{C}$ ) are embedded between the end-winding wires before the epoxy resin cures, whereas in the simulations the node is selected in the middle of the end-winding; highlighted with a black dot in Figure 10. The comparison was performed at two different mechanical angles: one at the coolant inlet ( $0^\circ$ ), and the second one at  $270^\circ$  along the coolant flow path. In order to estimate the temperatures at different mechanical angles, the network in Figure 10 was solved by considering appropriate coolant inlet temperature. From the heat flux ( $\dot{Q}_w$ ) removed by the coolant at the  $0^\circ$  slot, the coolant temperature rise may be obtained using (53), where  $\dot{m}$  and  $c_{p,w}$  are the coolant mass flow rate and specific heat capacity respectively.

$$\Delta T_{slot} = \frac{\dot{Q}_w}{\dot{m}c_{p,w}} \quad (53)$$

Assuming that the temperature increases linearly along the water jacket, the coolant inlet temperature at slot  $s$  is obtained from the expression  $T_{w,inlet}^s = s \Delta T_{slot} + T_{w,inlet}$ . The coolant temperature at the water jacket outlet is calculated by setting  $s = 120$ , which is the number of stator slots as given in Table 1. The simulated and measured coolant temperatures, at the inlet and outlet, are shown in Figure 12. It can be observed that the inlet coolant temperature is assumed to be constant in the simulation. The comparisons presented

in Figure 11 shows a good correspondence between the simulation and measurement results in transient and steady-state. The error in the steady state end-winding temperature estimation lies within 5%. The error observed in the estimated outlet coolant temperature, in Figure 12, is mainly due to the assumption of the constant inlet temperature instead of using the measurement data in the calculation. The magnet temperature estimation is not validated in this analysis.

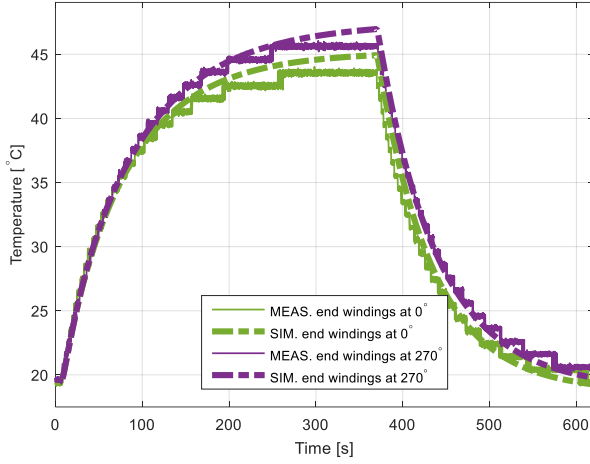


Figure 11. Comparison between measured and simulated temperatures for the 140 A DC test with coolant flow at 11 l/min in end-windings at 0° and 270° mechanical degrees.

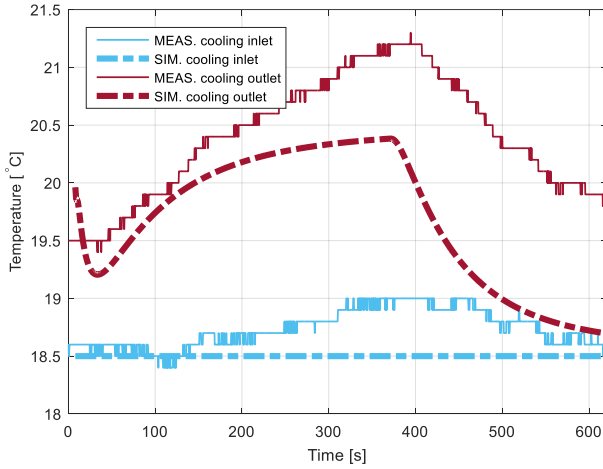


Figure 12. Comparison between measured and simulated temperatures for the 140 A DC test with coolant flow at 11 l/min at inlet-outlet sections of the cooling water jacket

## 2.Improved Efficiency Map and Loss calculations

The efficiency map is developed by calculating the losses at every torque  $T$  and speed  $\Omega$  combination in the motor torque-speed plane. The iron loss, friction loss and windage loss can be calculated from the operating speed of the motor, but the magnet and copper losses are functions of stator current which should be derived based on the electromagnetic torque. As the electromagnetic torque is also derived from the losses, the problem is formulated as a minimization problem given in (54) and MATLAB's `fmincon` function is used to get the

currents  $I_d$  and  $I_q$  that satisfies the constraints on maximum voltages ( $V_{max}$ ) and stator current ( $I_{max}$ ).

$$F = \left| T - \left( T_{em}(I_d, I_q) - \frac{P_c + P_{pm}(I_d, I_q) + P_{fr} + P_{wind}}{\Omega} \right) \right| \quad (54)$$

The thermal model captures the changes in magnet remanence and conductor resistance that affects the accuracy of efficiency calculation. The efficiency map in Figure.13 is obtained at constant temperature of 20° C for all the points. On the other hand, the efficiency map in Figure. 14 is calculated after achieving the steady-state temperature for magnet and winding at every operating point. The reasons for the mismatch is analyzed in detailed by performing a comparison study of losses.

The armature resistance increases with speed due to skin effect at low temperature, so the copper loss also increases with speed as shown in Figure.15. At high temperatures the contribution of AC loss reduces, but the overall copper loss in the torque-speed plane in Figure.16 increases as the permanent magnet flux linkage reduces in the  $d$  axis at high temperatures.

The hysteresis loss component in iron loss calculation is modelled as a function of speed while the eddy current loss varies with the square of speed. The same trend is observed in both Figures 17 and 18, but the increased magnet temperature at high speeds decreases the flux in the stator region as well as the iron loss.

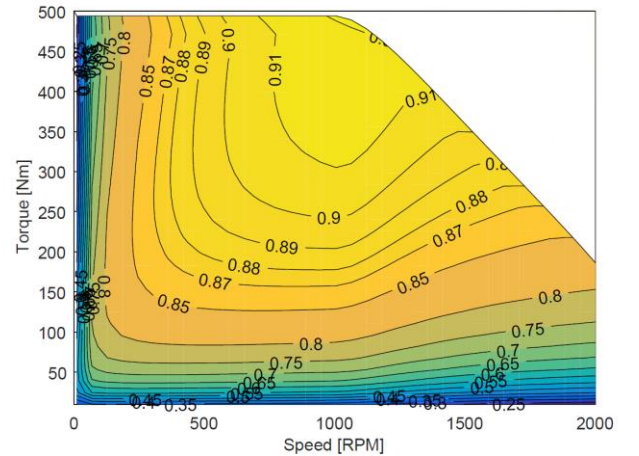


Figure 13. Efficiency map calculated with a fixed temperature (20 °C) for magnet and winding on the complete torque-speed plane



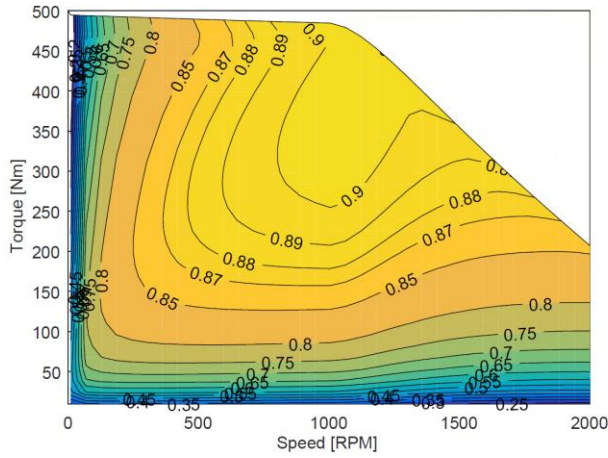


Figure 14. Efficiency map calculated with steady state temperature for magnet and winding at every operating point

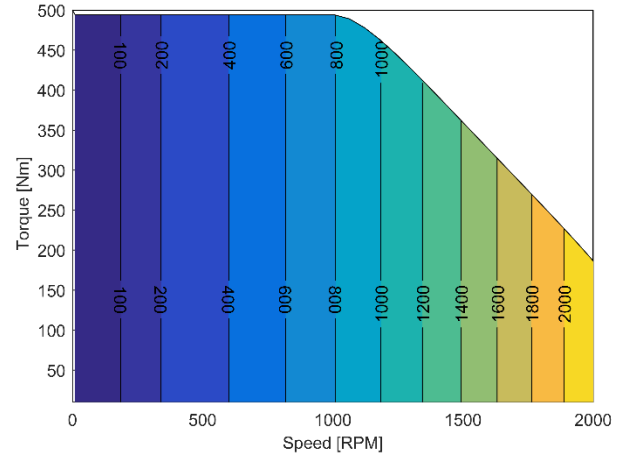


Figure 17. Iron loss calculated with a fixed temperature (20 °C) for magnet on the complete torque-speed plane

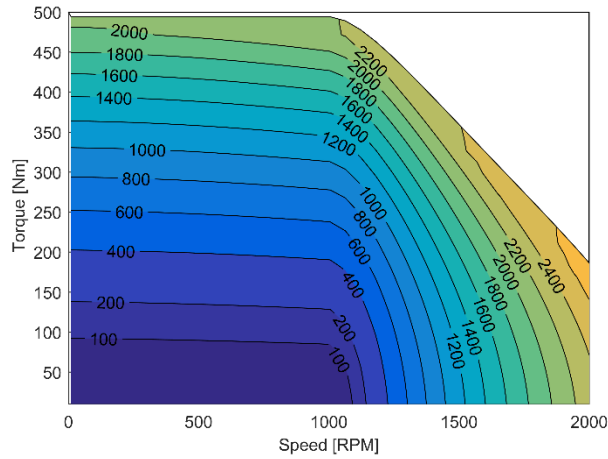


Figure 15. Copper loss calculated with a fixed temperature (20 °C) for magnet and winding on the complete torque-speed plane

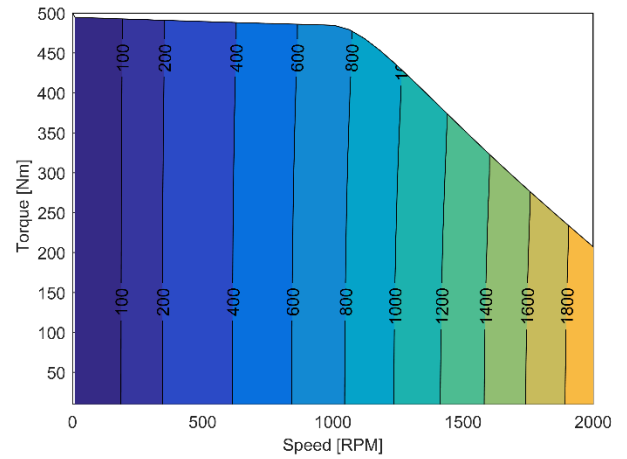


Figure 18. Iron loss calculated with steady state temperature for magnet at every operating point

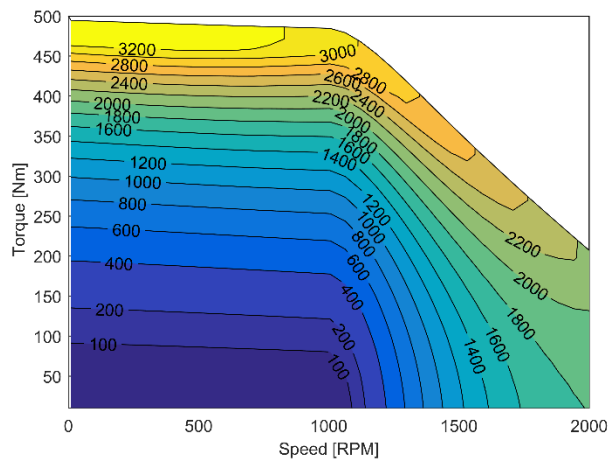


Figure 16. Copper loss calculated with steady state temperature for magnet and winding at every operating point

### 3. Driving cycle analysis

As the efficiency maps computed in the previous section show some differences, the influence of temperature on the real world operation of the motor should be understood. Therefore, the dynamic change of magnet and winding temperatures in New European Driving Cycle (NEDC) and its impact on the energy consumption is analyzed.

The vehicle parameters considered in the analysis are defined in Table 2 and the torque demand at the wheel ( $T_f$ ) is computed using (55) as the sum of aerodynamic resistance, gradient force, rolling resistance and inertial force. The required output torque of the motor is half of the torque demand shown in Figure 19 since there are two motors in the vehicle.

$$T_f = \left( m_v a + m_v g \sin \alpha + m_v g C_r \cos \alpha + \frac{1}{2} C_d \rho A v^2 \right) R_t \quad (55)$$

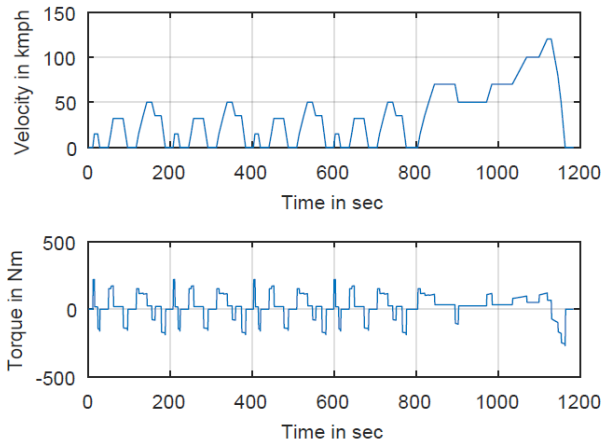


Figure 19 Vehicle speed and torque demand at the wheel for NEDC

The motor speed ( $\Omega$ ) is obtained from the reference speed of the vehicle in the driving cycle.

$$\Omega = \frac{v}{R_t} \quad (56)$$

In the generating mode, the electrical machine input power ( $P_{in}$ ) is defined by subtracting the machine loss from the traction power available at the wheel as in (57). The regeneration boundary can be obtained as shown in Figure 20 by assigning  $P_{in} = 0$  and by finding the maximum and minimum torque values at each speed numerically using the MATLAB fmincon function.

$$P_{in} = T_f \Omega - (P_a + P_c + P_{pm} + P_{ml}) \quad (57)$$

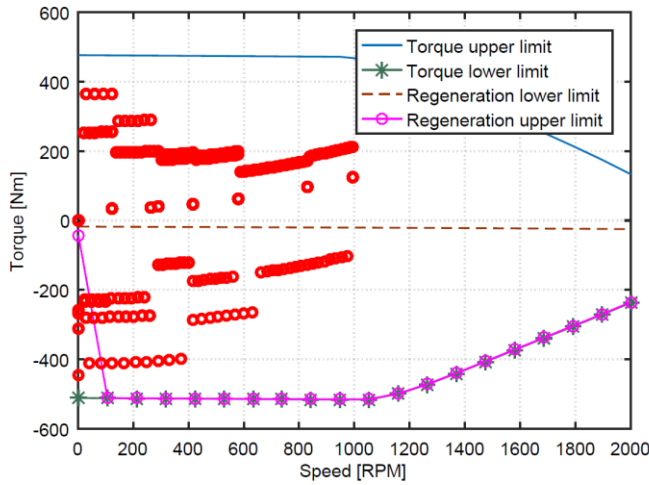


Figure 20 NEDC operating points in different regions of motor operation

When the motor operating points ( $T_f, \Omega$ ) in NEDC, marked with red circles in Figure 20, are in the region between the upper limit of regeneration and the torque axis, the required braking torque is given by mechanical brakes. Brake blending is not considered in this region. On the other hand, when the operating points are between upper and lower limits of the regeneration, the required braking torque is given by the electric motor itself. The battery is assumed to absorb all the recuperated energy from the motor.

In Figure 21, the temperature evolution, while simulating the NEDC for four times, is presented. The center of the end-winding and magnet temperatures (black and red nodes in Figure 10 respectively) are plotted along with the coolant outlet temperature. A heat exchanger in the thermal management system is used as an ideal component to reject a fixed amount of heat (2 kW) from the coolant. The machine reaches its thermal steady state already at the end of a single drive cycle. Though the coolant temperature is high in the plot, the end-winding temperature does not exceed 120°C and avoids a fast degradation of the wire insulation.

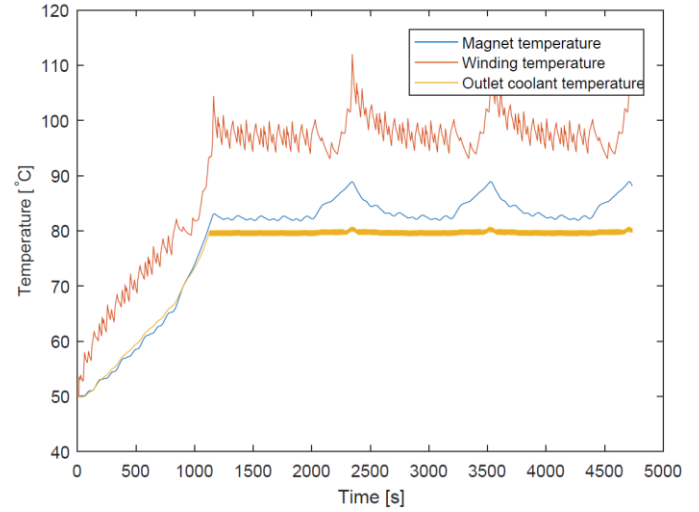


Figure 21 Temperature of magnet, winding, and coolant in NEDC

Table 2. Vehicle Parameters

Vehicle curb weight + driver ( $m_v$ )	2000 kg + 75 kg
Frontal Area (A)	2 m <sup>2</sup>
Co-efficient of drag ( $C_d$ )	0.4
Tire radius ( $R_t$ )	0.32 m
Rolling resistance coefficient ( $C_r$ )	0.01
No of in-wheel motors	2
Gradient	0 degrees

Electric power at the motor terminal is summed across the NEDC to get the net energy consumption. The analysis was repeated with and without thermal model and the results are given in Table 3. The difference in the calculated values of energy consumption can be minimized by considering average temperature in the driving cycle for magnet and winding without thermal model. Considering the tractive power is same in these analyses, the difference is caused only due to the variations in the motor losses. The study is repeated with different vehicle parameters as shown in Table 3.

Table 3. Energy consumption in New European Driving Cycle with two different vehicle weights.

	$m_v = 2075 \text{ kg}$	$m_v = 1875 \text{ kg}$
Energy consumption without thermal model	6.33 MJ	6.01 MJ
Energy consumption along with thermal model	6.46 MJ	6.12 MJ
Energy consumption considering average temperature in driving cycle without thermal model	6.43 MJ	6.08 MJ

## Conclusions

The influence of magnet and winding temperatures on the efficiency calculation of an outer rotor SPM machine was analyzed using a coupled electromagnetic-thermal model. The copper loss is high at low speed and high torque region due to its dependency on the winding temperature. It can be noted from the results that the iron loss in the stator is reduced as the magnet temperature increases. The change in the magnet loss is negligible in this motor. In order to assess the implication of the differences observed in the efficiency maps on a real world application, the energy consumption of an in-wheel motor electric vehicle in the NEDC was computed with and without the thermal model. The difference in energy consumptions shows that the thermal model is relevant and an accurate model is needed to capture the important phenomena. A rough but reasonable way to account for the temperature effects (without the LPTN thermal model) is to use the average driving cycle temperature for the magnet and winding in the electromagnetic model to obtain the efficiency map.

## References

1. Carter, F.W., "Note on Air-gap and Interpolated Induction," *J. Inst. Electr. Eng.* 925–933, 1900, doi:10.1049/jiee-1.1900.0095.
2. Carter, F.W., "The magnetic field of the dynamo-electric machine," *J. Inst. Electr. Eng.* 64(359):1115–1138, 1926, doi:10.1049/jiee-1.1926.0122.
3. Zhu, Z.Q., Wu, L.J., and Xia, Z.P., "An accurate subdomain model for magnetic field computation in slotted surface-mounted permanent-magnet machines," *IEEE Trans. Magn.* 46(4):1100–1115, 2010, doi:10.1109/TMAG.2009.2038153.
4. Žarko, D., Ban, D., and Lipo, T.A., "Analytical calculation of magnetic field distribution in the slotted air gap of a surface permanent-magnet motor using complex relative air-gap permeance," *IEEE Trans. Magn.* 42(7):1828–1837, 2006, doi:10.1109/TMAG.2006.874594.
5. Sprangers, R.L.J., Paulides, J.J.H., Gysen, B.L.J., and Lomonova, E.A., "Magnetic Saturation in Semi-Analytical Harmonic Modeling for Electric Machine Analysis," *IEEE Transactions on Magnetics*, ISBN 0018-9464 VO - 52, 2016, doi:10.1109/TMAG.2015.2480708.
6. Ilhan, E., Gysen, B.L.J., Paulides, J.J.H., and Lomonova, E.A., "Analytical hybrid model for flux switching permanent magnet machines," *IEEE Transactions on Magnetics*, ISBN 0018-9464 VO - 46: 1762–1765, 2010, doi:10.1109/TMAG.2010.2042579.
7. Ramakrishnan, K., Curti, M., Zarko, D., Mastinu, G., Paulides, J.J.H., and Lomonova, E.A., "A comparison study of modelling techniques for permanent magnet machines," *2016 Eleventh International Conference on Ecological Vehicles and Renewable Energies (EVER)*, IEEE, ISBN 978-1-5090-2464-3: 1–6, 2016, doi:10.1109/EVER.2016.7476424.
8. Romanazzi, P., Galizzi, V., Carbone, F., Miotto, A., and Howey, D.A., "Improved thermal equivalent circuit element applied to an external rotor SPM machine," *International Conference on Electrical Machine (ICEM)*, 2016.
9. Wrobel, R., Salt, D.E., Griffio, A., Simpson, N., and Mellor, P.H., "Derivation and scaling of AC copper loss in thermal modeling of electrical machines," *IEEE Trans. Ind. Electron.* 61(8):4412–4420, 2014, doi:10.1109/TIE.2013.2266088.
10. Zhu, Z.Q., Howe, D., and Chan, C.C., "Improved analytical model for predicting the magnetic field distribution in brushless permanent-magnet machines," *IEEE Trans. Magn.* 38(1 II):229–238, 2002, doi:10.1109/20.990112.
11. Ban, D. and Lipo, T.A., "Analytical Solution for Cogging Torque in Surface Permanent-Magnet Motors Using Conformal Mapping," 44(1):52–65, 2008.
12. Doncker, R. De, Pule, D.W.J., and Veltman, A., "Advanced Electrical Drives," Springer Netherlands, Dordrecht, ISBN 978-94-007-0179-3, 2011, doi:10.1007/978-94-007-0181-6.
13. Mellor, P., Wrobel, R., and Simpson, N., "AC Losses in High Frequency Electrical Machine Windings formed from Large Section Conductors," (2):5563–5570, 2014.
14. Žarko, Damir. "A systematic approach to optimized design of permanent magnet motors with reduced torque pulsations." PhD diss., Department of Electrical and Computer Engineering, University of Wisconsin-Madison, 2004.
15. Zarko, D., Ban, D., and Lipo, T.A., "Analytical solution for electromagnetic torque in surface permanent-Magnet motors using conformal mapping," *IEEE Trans. Magn.* 45(7):2943–2954, 2009, doi:10.1109/TMAG.2009.2014689.
16. Gieras, J.F. and Wing, M., "Permanent Magnet Motor Technology: design and applications," ISBN 978-1-4200-6440-7, 2002, doi:10.1201/9781420064414.
17. Boglietti, A., Member, S., Cavagnino, A., Staton, D., Shanel, M., Mueller, M., and Mejuto, C., "Evolution and Modern Approaches for Thermal Analysis of Electrical Machines," *IEEE Trans. Ind. Electron.* 56(3):871–882, 2009, doi:10.1109/TIE.2008.2011622.
18. Staton, D.A., Boglietti, A., and Cavagnino, A., "Solving the More Difficult Aspects of Electric Motor Thermal Analysis in Small and Medium Size Industrial Induction Motors," *IEEE Trans. Energy Convers.* 20(3):620–628, 2005, doi:10.1109/TEC.2005.847979.
19. Xu, B., Li, P., and Chan, C., "Extending the validity of lumped capacitance method for large Biot number in thermal storage application," *Sol. Energy*, 2012.
20. Romanazzi, P., Bruna, M., and Howey, D.A., "Thermal homogenisation of electrical machine windings applying the multiple-scales method," *ASME J. Heat Transf.* 139(January), 2017, doi:10.1115/1.4034337.

21. Huang, Z., Márquez-Fernández, F.J., Loayza, Y., Reinap, A., and Alaküla, M., “Dynamic Thermal Modeling and Application of Electrical Machine in Hybrid Drives,” *International Conference on Electrical Machines (ICEM)*, 2158–2164, 2014, doi:10.1109/ICELMACH.2014.6960483.
22. Kral, C., Haumer, A., and Bäuml, T., “Thermal Model and Behavior of a Squirrel-Cage Induction Machine for Traction Applications,” *IEEE Trans. Ind. Electron.* 55(10):3555–3565, 2008, doi:10.1109/TIE.2008.927242.

## Contact Information

Kesavan Ramakrishnan,

Politecnico di Milano,  
Via La Masa 1, 20156 Milano, Italy.  
Tel +39 349 050 5272  
[Kesavan.ramakrishnan@polimi.it](mailto:Kesavan.ramakrishnan@polimi.it)

## Acknowledgments

This paper is part of the ADvanced Electric Powertrain Technology (ADEPT) project which is an EU funded Marie Curie ITN project, grant number 607361. Kesavan Ramakrishnan and Pietro Romanazzi are Early Stage Researchers on this project.

## Definitions/Abbreviations

$B_r$	Magnet remanence (T)
$B_{slr}$	Slotless air-gap radial flux density (T)
$B_{sl\theta}$	Slotless air-gap tangential flux density (T)
$B_{sl}$	Slotted air-gap radial flux density (T)
$B_{s\theta}$	slotted air gap tangential flux density (T)
$\lambda$	Complex relative permeance
$\mu_0$	Permeability of air (Vs/(Am))

$\mu_r$	Relative permeability of iron
$p$	Number of pole pairs
$\alpha_p$	Magnet arc/pole pitch ratio
$Q_s$	Slot number
$l_m$	Magnet radial thickness (m)
$g$	Air gap length (m)
$R_g$	Radius of air gap center (m)
$R_r$	Radius of the rotor surface (m)
$R_m$	Radius of the magnet surface (m)
$R_s$	Stator outer radius (m)
$l_a$	stack length (m)
$b_0$	Slot opening (m)
$d_s$	Slot depth (m)
$N_c$	No. of conductors in a slot
$r, \theta$	Coordinates of air-gap evaluation points
$L_d, L_q$	Inductances in d-q axis (H)
$I_d, I_q$	Currents in d-q axis (A)
$m_v$	Vehicle mass (kg)
$C_d$	Drag coefficient
$A$	Frontal area of the vehicle (m <sup>2</sup> )
$\rho$	Density of Air (kg/m <sup>3</sup> )
$R_t$	Tire radius (m)
$v$	Vehicle velocity (m/s)
$C_r$	Coefficient of rolling resistance
$\alpha$	Gradient (rad)
$a$	Vehicle acceleration (m/s <sup>2</sup> )
$\Omega$	Motor speed (rad/s)
$T_f$	Tractive torque (Nm)
$T_{em}$	Electromagnetic torque (Nm)